Journal of Materials Chemistry C

ROYAL SOCIETY OF CHEMISTRY

PAPER

View Article Online
View Journal | View Issue

Cite this: J. Mater. Chem. C, 2020, 8, 13226

Unveiling interface interaction assisted broadband photoresponse of epitaxial 2D Bi_2O_2Se on perovskite oxides†

Yujie Guo, [a] Yekai Song,[bcd] Manli Yang,[a] Zhenyu Xu, [a] Haowei Xie,[a] Hui Li,[e] Zhuojun Li,*[bc] Huawei Liang, [a]* Shuangchen Ruan [a] and Yu-Jia Zeng [a]*

Received 9th July 2020,
Accepted 22nd August 2020

DOI: 10.1039/d0tc03245j

rsc.li/materials-c

Bi_2O_2Se has established itself as a revolutionary two-dimensional (2D) semiconductor owing to its superior electric, optoelectric and thermoelectric properties. The structural compatibility between Bi_2O_2Se and perovskite oxides makes the investigation of their heterointerfaces an intriguing frontier. Herein, we unveil the $Bi_2O_2Se/SrTiO_3$ interfacial interaction by studying the photoresponse of the oxide heteroepitaxy. The record-broad photosensitivity (365–1850 nm) is ascribed to a complex interplay between photoconductive, photogating, pyroelectric and photo-thermoelectric (PTE) effects. The distinctive pyroelectricity, which results in a 900-fold decrease in the response time, originates from the surface polarization and relaxation at the $Bi_2O_2Se/SrTiO_3$ interface. Self-powered behavior is reported for the first time in Bi_2O_2Se-based photodetectors. Under zero bias, the PTE-dominated photoresponse gives rise to a tunable polarity and magnitude of the photocurrent, and an estimated Seebeck coefficient of $-127.8\ \mu V\ K^{-1}$. The optimal photoresponsivity of 12.62 A W^{-1}, external quantum efficiency of 1424.08% and detectivity of 1.51×10^9 Jones indicate the performance advancement of the photodiodes based on as-grown Bi_2O_2Se. Our study sheds light on the exploitation of exotic physical phenomena at the heterointerfaces between Bi_2O_2Se and perovskite oxides, and also indicates that 2D Bi_2O_2Se has a wide range of applications in piezoelectrics, ferroelectrics, self-powered nanogenerators and optical communications.

Introduction

For over a decade, 2D materials have been considered as promising candidates for versatile applications in electronics, spintronics, and optoelectronics.[1–4] Among them, Bi_2O_2Se, with a zipper-like layered structure, has sparked interest owing to its distinctive physical properties featuring size-tunable bandgaps, high carrier mobility, ultrahigh yet broadband photosensitivity, low thermal conductivity and long-term ambient stability.[5–8] What makes Bi_2O_2Se more intriguing is its structural compatibility with perovskite oxides, such as $SrTiO_3$, $LaAlO_3$, (La,Sr)(Al,Ta)O_3, and yttria-stabilized zirconia (YSZ) and $Bi_2Sr_2Ca_{n-1}Cu_nO_{2n+4+x}$ series high transition temperature superconductors (HTSCs).[9,10] Their heterogeneous integration with Bi_2O_2Se enables coupling of the physical functionalities of the two counterparts, including optoelectronics, multiferroics, magnetoelectrics, neuromorphics, ferroelectrics and HTSCs.[9,11–13] Moreover, the epitaxial heterointerfaces offer potential for exotic physical phenomena such as 2D electron gas (2DEG), quantum transport, superconductivity and spin-dependent transport at magnetic tunnel junctions.[9,10,14]

Despite being an important frontier, comparatively little is known about the interface interaction between Bi_2O_2Se and perovskite oxides. Nevertheless, considerable discussions have focused on their respective surfaces and interfaces, ranging from carrier dynamics to atomic arrangement. The most intriguing example is 2DEG at the heterojunction of perovskite oxides, which exhibits an extremely high carrier mobility of over $10^4\ cm^2\ V^{-1}\ s^{-1}$ and an electron density of up to $10^{14}\ cm^{-2}$.[15,16] These heterointerfaces reach a high level of competiveness in transistors, optoelectrics, memory devices, superconductivity and ferromagnetism.[15–18] The origin of 2DEG has been debated, attributed either to the "polar catastrophe" mechanism due to the

[a] Key Laboratory of Optoelectronic Devices and Systems, College of Physics and Optoelectronic Engineering, Shenzhen University, Shenzhen, 518060, P. R. China. E-mail: yjzeng@szu.edu.cn, hwliang@szu.edu.cn
[b] State Key Laboratory of Functional Materials for Informatics, Shanghai Institute of Microsystem and Information Technology, Chinese Academy of Sciences, Shanghai, 200050, P. R. China. E-mail: lizhuojun@mail.sim.ac.cn
[c] CAS Center for Excellence in Superconducting Electronics (CENSE), Shanghai 200050, P. R. China
[d] School of Physical Science and Technology, ShanghaiTech University, Shanghai 200031, P. R. China
[e] College of Engineering Physics, Shenzhen Technology University, Shenzhen 518118, P. R. China

† Electronic supplementary information (ESI) available. See DOI: 10.1039/d0tc03245j

polarity discontinuity across the interface,[15,19] or to the abundant free electrons generated by the oxygen vacancies on the $SrTiO_3$ surface.[20,21] Either way, the $SrTiO_3$ substrate with TiO_2 termination is essential for the creation of 2DEG. Hence, the surface stoichiometry of $SrTiO_3$ has been atomically resolved, demonstrating a slight coordination deviation owing to the structural rearrangement.[22] This surface structure gives rise to an intrinsic polarization and further surface pyroelectricity in $SrTiO_3$, which could be artificially tuned by SiO_2 capping, light pulse, elemental substitution and strain gradients.[12,22,23] Considering Bi_2O_2Se, its electrical and magnetotransport properties are dominated by scattering among the surface-accumulated electrons with quasi-2D behavior.[24] Intensive interlayer phonon scattering effectively promotes the electron–phonon transport, whereas scattering with ionized defects is prohibited by the self-modulated doping of the layered structure.[25,26]

Here, we take a step forward by investigating the interface interaction of epitaxial Bi_2O_2Se on $SrTiO_3$. To this end, critical discussion has been done on the light–matter interaction of the heteroepitaxy between Bi_2O_2Se and $SrTiO_3$, both of which are appealing for broadband photon detection.[27,28] Specifically, Bi_2O_2Se presents one of the best photoresponses among 2D semiconductors, particularly in terms of the responsivity (R), external quantum efficiency (EQE) and photosensitive band.[29] The superior performance arises individually or congruously from the photoconductive, photovoltaic, photogating and bolometric effects, whereas the PTE one lacks sufficient quantitative investigation.[29–31] On the other hand, $SrTiO_3$ photodetectors achieve an ultrabroad spectral response extending to the long-wavelength infrared (LWIR) region owing to their high Seebeck coefficient and strong sub-bandgap absorption related to the Ti–O longitudinal phonon mode.[32] In our devices based on the heteroepitaxy of the above two, a record-broad detection band (365–1850 nm), a photoresponsivity of 12.62 A W^{-1}, an external quantum efficiency of 1424.08% and a detectivity of 1.51×10^9 Jones are obtained. The generation of photocarriers is synergistically governed by the photon- and thermal-induced effects. A distinctive pyroelectric effect is identified in the centrosymmetric system, arising from the polarization and relaxation at the $Bi_2O_2Se/SrTiO_3$ interface, according to the atomic-level observation and density functional theory (DFT) calculation. The emerging self-powered photoresponse is governed predominantly by the PTE effect, in which the interface scattering and phonon coupling play crucial roles. Remarkably, the tunable magnitude and polarity of the photocurrent and the estimated high Seebeck coefficient of -127.8 μV K^{-1} indicate that Bi_2O_2Se shows great promise in low-power optoelectrics and thermoelectrics.

Experimental

Growth of Bi_2O_2Se layers

Bi_2O_2Se layers were deposited by pulsed laser deposition (PLD), with the experimental details reported elsewhere.[33] Specifically, a polycrystalline Bi_2O_2Se target was prepared from Bi_2O_3 (4N), Se (4N) and Bi (4N) powders. Initially, the powders were loaded into an Al_2O_3 crucible, and sealed using an evacuated tube. The powders then underwent thermal treatment at 950 °C for 24 h. After naturally cooling down, the as-sintered precursor was ground thoroughly in an argon-filled glovebox before calcination in a hot-pressing furnace at 450 °C/6 MPa for 12 h under a continuous argon flow. The obtained Bi_2O_2Se targets with high density were loaded into the PLD chamber for the growth of Bi_2O_2Se thin films on $SrTiO_3(001)$ single crystal substrates. During the high vacuum deposition, a 248 nm wavelength laser beam was excited using a KrF excimer laser (Coherent, COMPexPro201). The chamber pressure, energy density, repetition rate and target-substrate distance were $\sim 10^{-5}$ Pa, 15 mJ mm^{-2}, 4 Hz and 50 mm, respectively. The substrate temperature was set to 425 °C to achieve the optimal deposition conditions, and the deposition rate was 0.25 Å per pulse. The films were patterned to a dimension of 3 mm × 0.5 mm using a metal mask during the growth, as shown in Fig. S1 (ESI†).

Structural characterization

XRD measurement was conducted on an X-ray diffractometer (XRD, Bruker, D8 Discover) with Cu Kα radiation in a high-resolution mode. Raman spectra were recorded on a micro-confocal Raman spectrometer (HORIBA LabRAM HR Evolution) under excitation with a 514 nm laser. The cross-section of the $Bi_2O_2Se/SrTiO_3$ interface was characterized by transmission electron microscopy (TEM, JEOL, JEM-ARM300F). Its atomic arrangement was inspected by high-angle annular dark-field scanning transmission electron microscopy (HAADF-STEM) using a double spherical aberration probe corrector. The surface morphology and layer thickness of the Bi_2O_2Se layers were inspected by atomic force microscopy (AFM) on an AIST scanning probe microscope (SPM).

Device fabrication

Two-terminal $Bi_2O_2Se/SrTiO_3$ photodetectors were fabricated by directly depositing metallic indium, whereas a Bi_2O_2Se/Si photodetector was prepared by transferring the pre-patterned Bi_2O_2Se layer onto a Si substrate. The latter involves two procedures – region-selective wet-chemical etching and polystyrene (PS)-assisted transferring process. As for selective etching, 100 nm thick poly(methyl-methacrylate) (PMMA, MicroChem, 950 kg mol^{-1}) was spin-coated onto the Bi_2O_2Se grown $SrTiO_3$ substrate at a speed of 4000 rounds per minute (rpm) for 45 s and then baked on a hot plate at 150 °C for 3 min. Then the substrate was subject to a standard e-beam lithography (EBL) procedure in a Raith PIONEER two system. The developed $Bi_2O_2Se/SrTiO_3$ substrate was exposed to oxygen plasma for 30 s, and then steeped into a mixed etchant with a $H_3O^+ : H_2O_2 : H_2O$ atomic ratio of 2 : 4 : 8 for 45 s. The substrate was transferred into a beaker full of deionized (DI) water and then rinsed several times before blow-drying by floating nitrogen.[34] In terms of the transferring process, the patterned wafer was spin coated by PS at 3500 rpm for 60 s and then baked on a hot plate at 85 °C for 15 min. After cutting away the edge of the PS layer, the PS-coated sample was peeled off with the assistance of a drop of DI water. The film was then transferred onto a Si substrate, and baked at 80 °C for 1 h and

subsequently at 150 °C for 30 min in order to increase the adhesion between Bi_2O_2Se and the Si substrate. Finally, the substrate was immersed in toluene for one day and then acetone for 5 h to remove the organic residues before blow-drying by floating nitrogen. Device implementation was completed by depositing Au electrodes onto the transferred Bi_2O_2Se layer *via* procedures including EBL, metal sputtering and lifting-off.

Photoresponse measurement

Laser radiation in a wavelength range spanning from 365 nm to 1064 nm was carried out using continuous wave (c.w.) lasers, while the counterpart from 1100 nm to 1850 nm was done by pulsed lasers. The incident power at each wavelength was tested using a calibrated power meter. The lasers were focused onto the selected positions of the channels at a distance of 1.5 cm above the photodetectors, and the beam diameters were kept at the same level (approximately 2 mm). The *I*–*V* and *I*–*t* curves of the photodetectors were measured using Keysight B2902A and Keithley 4200 semiconductor analyzers when illuminated by the c.w. lasers and the pulsed lasers, respectively.

DFT calculation

DFT simulation was performed by using the CP2K package.[35] The PBE functional[36] with Grimme D3 correction[37] was used to describe the system. Unrestricted Kohn–Sham DFT was used as the electronic structure method in the framework of the Gaussian and plane-wave method.[38,39] Goedecker–Teter–Hutter (GTH) pseudopotentials[36,40] and DZVPMOLOPT-GTH basis sets[38] were utilized to describe the molecules. A plane-wave energy cut-off of 500 Ry was employed. All the atoms were relaxed during geometry optimization. For the slab model, a vacuum of 15 Å was added along the *z* direction. For the $Bi_2O_2Se/SrTiO_3$ system, no vacuum was used. We used a 9 atomic layer $p(4 \times 4)$ $SrTiO_3$ and a 5 atomic layer $p(4 \times 4)$ Bi_2O_2Se. The simulation box was $15.729 \times 15.708 \times 35.636$ Å^3.

Results and discussion

Ultrabroad photosensitive band

Fig. 1a depicts the body-centered tetragonal crystallographic structures of Bi_2O_2Se and $SrTiO_3$ aligned along the *c*-axis, which demonstrates their structural compatibility with only 0.51% lattice mismatch. The cross-sectional STEM image in Fig. 1b confirms the nice epitaxy with a well-defined $Bi_2O_2Se/SrTiO_3$ interface of atomic flatness. Fig. 1c shows the typical XRD spectrum of the Bi_2O_2Se layer, which presents only sharp peaks corresponding to the Bi_2O_2Se (00*l*) and $SrTiO_3$ (00*l*) reflections.

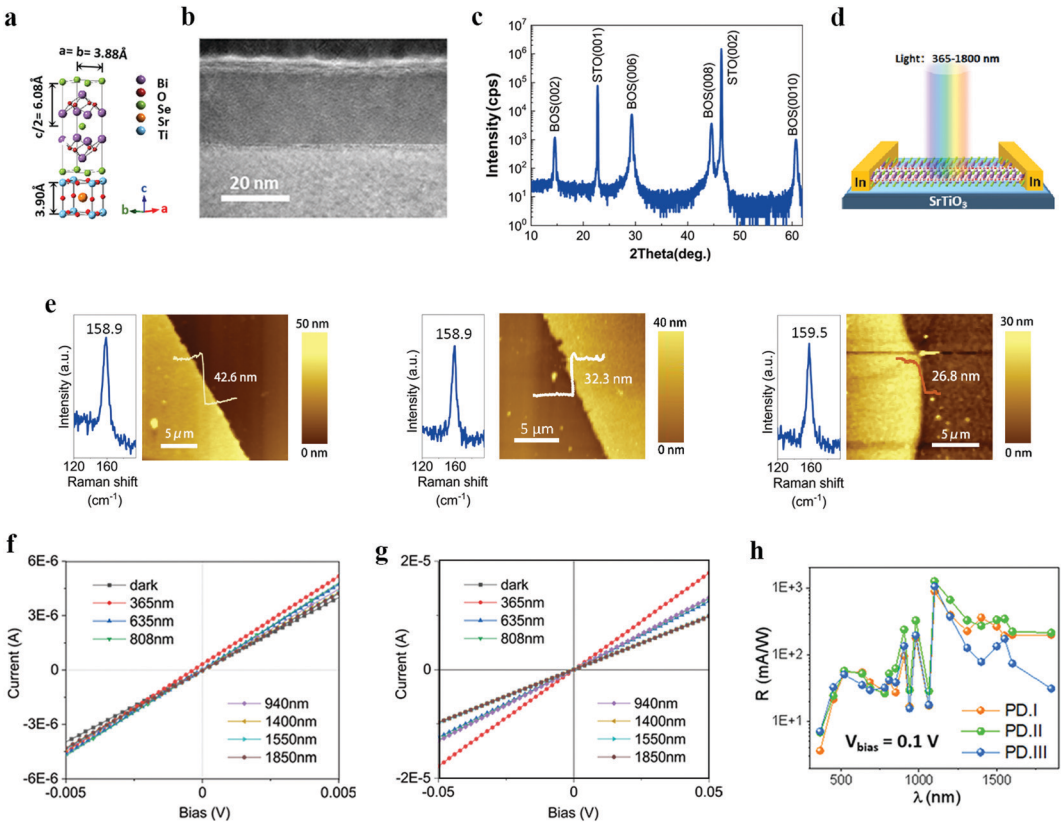

Fig. 1 Broadband photoresponse of the $Bi_2O_2Se/SrTiO_3$ photodetectors. (a) Schematic of the tetragonal crystallographic structures of Bi_2O_2Se and $SrTiO_3$. (b) Cross-sectional STEM image of the $Bi_2O_2Se/SrTiO_3$ interface. (c) XRD spectrum of the as-grown Bi_2O_2Se on the $SrTiO_3$ substrate. (d) Scheme of the devices under light excitation. (e) AFM images and the corresponding Raman spectra of the Bi_2O_2Se layers with thicknesses of 42.6 nm, 32.3 nm, and 26.8 nm. (f and g) *I*–*V* curves under the dark and laser radiation conditions of (f) PD.I and (g) PD.III. (h) Wavelength (λ) dependence of responsibility (*R*) when illuminated by lasers with wavelengths ranging from 365 nm to 1850 nm under 0.1 V bias.

This preferential orientation of layer growth also reflects the epitaxial growth, and can be verified by more comprehensive XRD and AFM characterization.[33] The architecture of the $Bi_2O_2Se/SrTiO_3$ photodetectors is illustrated in Fig. 1d, with a channel length of 0.5 mm (Fig. S1, ESI†). The device manufacturing process skips the challenging step of transferring Bi_2O_2Se, which impedes the contamination and quality degradation of the crystal. As indicated by the AFM images in Fig. 1e, three typical thicknesses were chosen −42.6 nm, 32.3 nm, and 26.8 nm. As shown in Fig. 1e, a single peak at ∼159 cm^{-1} is present in the corresponding Raman spectra, which is associated with the A_{1g} phonon mode of Bi_2O_2Se. Within this thickness region, the Hall mobility (μ_{Hall}) of the layers shows a proportional dependence on their thicknesses.[33] In other words, the minimal μ_{Hall} was obtained at a thickness of 26.8 nm, while the μ_{Hall} saturates at 42.6 nm. Here, we name these devices as PD.I, PD.II and PD.III in a descending thickness sequence. As shown in Fig. 1f and g, the measured current-*versus*-voltage (*I*–*V*) curves always exhibit perfect linearity in the presence or absence of the excitation of lasers, whose incident powers (P) are plotted as a function of laser wavelengths (λ) in Fig. S1 (ESI†). This scenario suggests the nice Ohmic contact between the Bi_2O_2Se layer and the electrodes, which also excludes the photovoltaic effect with a typical rectifying behavior. Over a broad region from 365 nm to 1850 nm, the photocurrent ($I_{ph} = I_{light} - I_{dark}$) can be detected under an external bias of 0.1 V, where I_{light} and I_{dark} represent the current measured in the presence and absence of light illumination, respectively. To the best of our knowledge, this photosensitive band is the widest among all the Bi_2O_2Se based photodetectors. For better evaluation of the device performance, the other key figures of merit of the photodetectors, namely, R, EQE and D^* are derived as shown in Fig. 1h and Fig. S2 (ESI†), respectively. Their definitions are expressed as:

$$R = \frac{I_{ph}}{p \cdot A} \quad (1)$$

$$\mathrm{EQE} = \frac{I_{ph}/(A \cdot e)}{p/h\nu} \quad (2)$$

$$D^* = R\sqrt{\frac{A}{2eI_{dark}}} \quad (3)$$

where p, A, e, h, ν are the incident power density, the effective channel area, the elementary charge, the Planck constant and the frequency of the incident laser, respectively.

When exploiting the underlying mechanisms of photon detection, the photoconductive effect from Bi_2O_2Se is unquestionably involved. Moreover, the photogating effect also contributes to the I_{ph} generation, as shown in Fig. S3 in the ESI.† Aside from these photon-induced origins, we expect the role of other effects originating from the radiation-induced heat or the inter-band defect states. This assumption is made based on three facts: (i) the broadband photoresponse is beyond the bandgap of Bi_2O_2Se (0.85 eV);[28] (ii) the *R*–*P* relationship is occasionally non-linear, as shown in Fig. S4 (ESI†); and (iii) the properties of PD.I scarcely outperform those of the other two (Fig. 1h and Fig. S2, ESI†), despite its highest electric conductivity and strongest light absorptivity,[28,33] both of which facilitate a photon-induced photoresponse. On the other hand, the contribution of the defect states could be precluded as (i) the dominant shallow donors in the $[Se]_n^{2n-}$ layers are spatially separated from the electron conduction channels – $[Bi_2O_2]_n^{2n+}$ layers[33,34,41,42] and (ii) the band tails, surface dangling bonds or Fermi-level pinning are naturally suppressed in Bi_2O_2Se.[5,24,26,30,43] Hence, the thermal-related effects are expected to participate in the photoresponse, which will be verified in the following context.

Instant photoresponse induced by pyroelectricity

The time-resolved photoresponse was measured by manually turning on and off the laser. As displayed in Fig. 2a, the time-*versus*-current (*I*–*t*) curve displays a four-stage current variation when excited by a laser at 365 nm. Specifically, instantaneously upon light irradiation, an abrupt current increase occurs and then immediately decays to a steady plateau (marked as stage I in Fig. 2a). When turning off the laser, a peak of reversed direction appears owing to the instant current decrease. Eventually, the current goes back to the I_{dark} value. This process indicates the typical characteristic of pyroelectricity, in which a transient charge release arises from the variation of spontaneous polarization in the material owing to the fluctuation of the temperature. For further substantiation, the decay curve at stage I is fitted nicely to $I \propto \sqrt{t}$, which fulfills the protocol for the pyroelectricity of a thin polar layer on a thick dielectric substrate.[23,44] With the assistance of the pyroelectric effect, the light sensing capability is strengthened, particularly the response time. As plotted in Fig. 2b, τ_1 is defined as the duration for I_{ph} to reach the first pyroelectric peak after the light stimuli, whereas τ_2 is defined as the duration for I_{ph} to reach 90% of the saturation value. As compared in Fig. 2c, regardless of the radiant λ, τ_1 is constantly lower than τ_2, reaching a maximal decrease of 900 fold. Nevertheless, in terms of R, D^* and EQE, a notable enhancement by the pyroelectricity is only observed under laser excitation at 365 nm by a maximal factor of 1.64, whereas a contrasting trend is observed under visible light illumination (405–685 nm, as shown in Fig. S5, ESI†). This unconventional scenario is attributed to the planar-electrode configuration with a large channel dimension, in which abundant evanescent photocarriers excited by the pyroelectric process were sacrificed *via* recombination and trapping during the long journey towards electrodes.[30]

Critical discussion has been made on the origin of pyroelectricity in a centrosymmetric crystallographic system of Bi_2O_2Se and $SrTiO_3$. As shown in Fig. 2d–f, double peaks are commonly observed in the *I*–*t* curves within the first second of laser excitation at 405–520 nm. This distinctive phenomenon implies that more than one components are involved in the pyroelectricity. Under optimal exposure of the same λ, the performance of PD.I–III relies highly on the Bi_2O_2Se thickness (δ). As δ increases, the response time and intervals between the two current peaks vary proportionally. Also, the pyro-induced current enhancement is more profound with lower δ. These phenomena

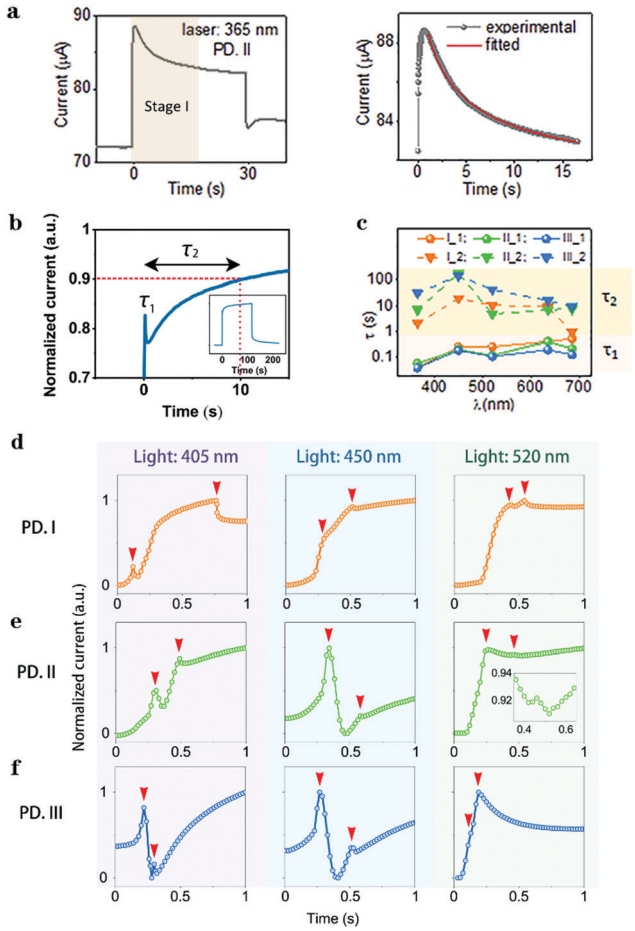

Fig. 2 Transient photoresponse under laser radiation and 0.1 V bias. (a) Left: the I–t curve of PD.II under illumination at 365 nm, showing a typical 4-stage characteristic of the pyroelectric effect; right: fitting the left I–t curve at stage I to $I \propto \sqrt{t}$, in which the grey dots indicate the measured data, while the red curve represents the fitted line; (b) schematic of the response time τ_1 and τ_2; (c) comparison of τ_1 and τ_2 in PD.I–III under irradiation in the UV and visible light regions (365–685 nm); the I–t curves of (d) PD.I, (e) PD.II, and (f) PD.III within the first second of laser excitation with λ values of 405 nm, 450 nm and 520 nm, respectively.

elucidate that pyroelectricity is more prominent in the photodetectors with lower δ, which indicates stronger interfacial energy transfer and thermal dissipation.[45] When transferring the as-grown Bi_2O_2Se onto the Si substrate,[41] as displayed in S5 in the ESI,† this peculiar double current scenario vanishes, suggesting the crucial role of the $Bi_2O_2Se/SrTiO_3$ interface in the pyroelectric process. It is also worth mentioning that pyroelectricity is a robust property in our devices showing no noticeable performance degradation after over 50 circles of tests.

To figure out the fundamental origin at the $Bi_2O_2Se/SrTiO_3$ interface that triggers the pyroelectricity, the atomic arrangement at the interface was inspected by cross-sectional STEM. As shown in Fig. 3a, the bright dots are correlated to the atoms in Bi_2O_2Se and $SrTiO_3$ on the right, where oxygen atoms are too light to be seen. The perfect atom-to-atom alignment at the $Bi_2O_2Se/SrTiO_3$ interface is in accordance with the overlapped patterns in the Fast Fourier Transform (FFT) diffractogram, confirming the heteroepitaxy. As consistent with the previous observations,[22,23] the atomically flat interface is terminated by the $[Bi_2O_2]^{2+}$ and TiO_2 layer, respectively, ensuring a strong interfacial lattice interaction. The dots in the first few lattice planes closest to the interfaces exhibit noticeably enlarged diameters and distorted shapes. This indicates the minor shift of atoms from their theoretical sites. A more intuitive indication is given by the intensity profile plotted from the area marked by a yellow square as shown in Fig. 3a. On the $SrTiO_3$ side, the first three peaks closest to the interface, which are correlated to the Sr lattice planes, show an ascending intensity towards the interface. This reveals the exaggerated degree of atom shifting, directly relevant to the surface polarization. The corresponding polar thickness (1.2 nm) is in good agreement with the theoretical estimation.[23] The surface polarization of $SrTiO_3$ gives rise to surface pyroelectricity,[23] which testifies our previous observations. On the Bi_2O_2Se side, the disturbed structural periodicity and the distorted column shapes are more evident, particularly within the first four lattice planes nearest to the interface. As revealed in the intensity profile, the peak intensity is lower, and the lattice spacing is enlarged, which demonstrates the surface polarization of Bi_2O_2Se. The structural imperfections, for instance, at the area marked in

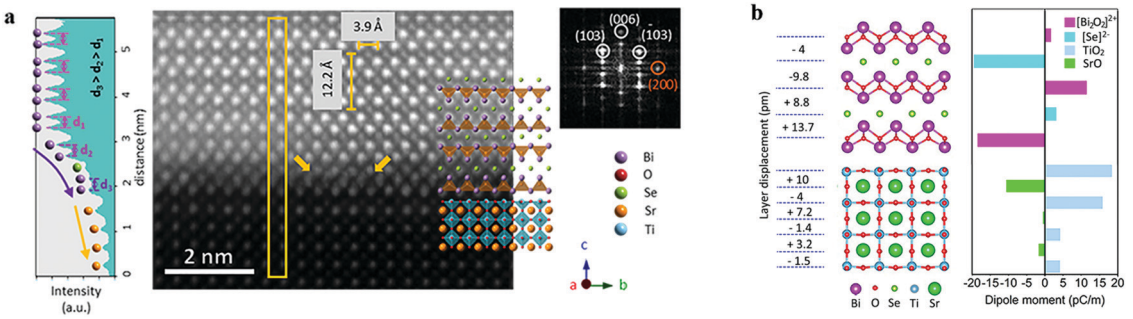

Fig. 3 Structural rearrangement at the $Bi_2O_2Se/SrTiO_3$ interface. (a) Middle: Cross-sectional STEM image of the $Bi_2O_2Se/SrTiO_3$ interface, with the lattice spacing and corresponding atom columns indicated; left: the line profile extracted from the yellow-framed square in the image; right: the FFT diffractogram in which the diffracted spots corresponding to Bi_2O_2Se and $SrTiO_3$ are marked in white and orange circles, respectively; (b) DFT-calculated displacement of crystal planes (pm) and the dipole moment per unit surface area (pC m^{-1}) at the $Bi_2O_2Se/SrTiO_3$ interface.

yellow arrows, can be attributed to the native point defects, namely, O vacancies (V_O), Se vacancies (V_{Se}) and Bi antisites at the Se sites (Bi_{Se}) that are formed during PLD.[24]

The interfacial polarization and relaxation were further quantified by DFT simulation.[35–40,46] In the bulk $SrTiO_3$ and Bi_2O_2Se, neither net charge nor polar lattice distortion is present. On the $SrTiO_3$ surface without Bi_2O_2Se capping, the top most TiO_2 plane moves inwards with respect to its theoretical sites, whereas the top most SrO plane moves outwards. The lattice distortion is induced by the surface relaxation. The resultant surface dipoles per unit surface area are -73.5 pC m^{-1} and 4.2 pC m^{-1} in the TiO_2 and SrO planes, respectively. These considerable statistics agree excellently with the previous measurements, which supports the validity of our model.[23] Bi_2O_2Se interacts with $SrTiO_3$ forming a heterogeneous structure, and the calculated lattice displacement and the dipole moment of each plane are listed in Fig. 3b. The polarization of the $SrTiO_3$ surface decreases, yet retains a considerable net dipole moment of 29.8 pC m^{-1}. This value is comparable to that extracted from the $SrTiO_3$ surface by low energy electron diffraction (LEED), where the surface polarization close to the strongly polar materials is detected.[23] In the Bi_2O_2Se counterpart, a more drastic lattice displacement occurs mainly within the two $[Bi_2O_2]^{2+}$ and $[Se]^{2-}$ layers closest to the surface, which coincides with our STEM observation. The resultant net dipole moment (-21.6 pC m^{-1}) is in the reversed direction to that on the $SrTiO_3$ surface.

With the aforementioned experimental observations and DFT simulations in mind, we sketch the dynamics of the pyroelectric process in the $Bi_2O_2Se/SrTiO_3$ photodetectors as shown in Fig. 4. Unlike the conventional pyroelectricity that requires a non-centrosymmetric crystallographic structure, the origin of our centrosymmetric $Bi_2O_2Se/SrTiO_3$ system is associated with interfacial polarization. At room temperature (Fig. 4a), spontaneous polarization occurs within the first few lattice planes of Bi_2O_2Se and $SrTiO_3$ at the interface owing to the surface relaxation. The localized dipoles randomly oscillate in a small degree with respect to the aligned axes, leaving free charges accumulated on both surfaces. Upon laser radiation (Fig. 4b), the abrupt temperature increase in Bi_2O_2Se ($dT_{(Bi_2O_2Se)}/dt > 0$) disturbs its surface dipole oscillation towards a more drastic degree. The resultant net polarization in the direction perpendicular to the interface is diminished, and accordingly the amount of free charges on the Bi_2O_2Se surface decreases.[9]

This instant fluctuation of the surface charge concentration is associated with the emergence of the first pyroelectric current (I_{pyro}) peak in the *I–t* curve, whereas I_{pyro} vanishes when the temperature in the Bi_2O_2Se layer gets stabilized. Simultaneously, heat dissipation towards the $SrTiO_3$ substrate occurs at the interface in order to establish a thermal equilibrium, such that the temperature variation on the $SrTiO_3$ surface ($dT_{(SrTiO_3)}/dt > 0$) generates a second pyroelectric process, as shown in Fig. 4c. If the heat transfer across the interface takes a longer time than the first pyroelectric process, double I_{pyro} peaks are observed. Otherwise, the two peaks are merged into one.

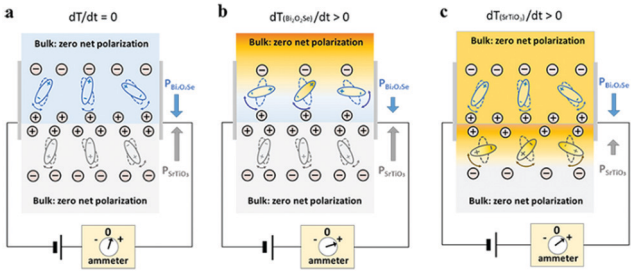

Fig. 4 Mechanism of the pyroelectric process in the $Bi_2O_2Se/SrTiO_3$ photodetectors. (a) In the dark, the surface polarization at the $Bi_2O_2Se/SrTiO_3$ interface results in random oscillation of electric dipoles and surface charge accumulation; the ellipses represent the electric dipoles, whereas the circle with a subtraction or plus sign refers to the electron or hole; (b) immediately after light illumination, the dramatically oscillated electric dipoles and diminished surface charges in the Bi_2O_2Se layer around the interface are associated with the sudden temperature fluctuation induced by laser irradiation; (c) right after the heat transfer across the interface, dramatically oscillated electric dipoles and diminished surface charges originate from the temperature fluctuation on the $SrTiO_3$ surface after laser irradiation.

PTE-triggered self-powered behavior

To individually study the thermal-induced effects at equilibrium, a photoresponse at zero bias was detected, since the photoconductive and photogating effects are external-bias oriented, and the pyroelectricity is a transient effect. As depicted in Fig. 5a, in an attempt to create a larger temperature gradient across the channel, the length was redefined as the length of the Bi_2O_2Se layer (3 mm). These devices were named as PD.I′–III′ in a descending δ sequence. A laser at 365 nm with tremendously higher power density was used for excitation in order to exaggerate the thermal-induced photoresponse.[31] As shown in Fig. 5b, the excellent on–off repetition in the *I–t* curves confirms the self-powered light sensing ability. When sweeping the laser longitudinally across the channel, the current shows a tunable polarity and magnitude with respect to the laser radiant position. Here, we define the Bi_2O_2Se/electrode interface that eventually connects to the positive channel of the ammeter as the positive end, and *vice versa*. Notably, the maximal absolute values of the current are always achieved upon light illumination at the two ends, where the highest temperature asymmetry is present owing to the localized heating induced by laser irradiation.[32] This is the typical characteristic of the PTE effect governed by the temperature gradient.[28,47] The current flows in the direction following the contact polarity of the illuminated end due to the n-type semiconducting characteristic of Bi_2O_2Se. To elaborate, under laser irradiation at the positive end (Fig. 5a), the positive current flow is driven by the internal PTE potential (ε_{PTE}) pointing from the positive end to the negative, and *vice versa*. The same dependence on the current polarity and magnitude is observed when subjected to an external bias, as shown in Fig. S6 (ESI†).

A proportional correlation between I_{ph} and δ is revealed in Fig. 5b, so between *R*, *D**, and EQE, as demonstrated in Fig. S7 (ESI†). To explain the strong δ dependence on the device performance, three key factors facilitating the PTE effect should be taken into account – higher electrical conductivity (σ), higher

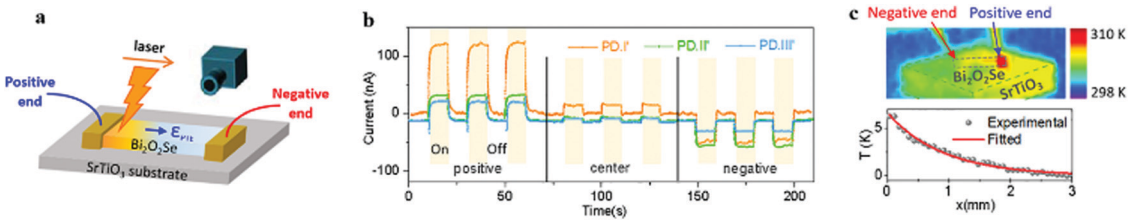

Fig. 5 Photoresponse triggered by the PTE effect. (a) Scheme of the $Bi_2O_2Se/SrTiO_3$ photodetector with a longer-channel configuration and a monitored temperature gradient in the channel using an IR camera, in which the internal photothermo-electric potential (ε_{PTE}) is directed; (b) I–t curves of PD.I′–III′ under zero bias after optical exposure at the negative and positive ends and in the centre; (c) temperature landscape of PD.I′ when illuminated at the positive end on top and the extracted temperature profile in the bottom.

Seebeck coefficient (S) and higher temperature gradient.[32] The critical role of σ is testified by the positive correlation between δ and σ, especially the strong interface scattering and carrier localization in PD.III′ owing to the poor layer continuity.[33] As shown in S7 in the ESI,† the predominant impact of S is excluded based on semiclassical Boltzmann transport theory.[26,48] In terms of the temperature gradient, it contributes to the drastic performance enhancement in PD.I′ compared to PD.II′. The interface thermal conductivity (κ) of Bi_2O_2Se is more than 20 times higher than its intrinsically low in-plane κ, which is ascribed to the low phonon group velocity, strong anharmonicity and large Gruñeisen parameters.[26,44,45,49] Particularly in our cases, the interface phonon coupling and scattering can be further strengthened by the structural epitaxy, elevated interface adhesion by the PLD process and lattice strain induced by defects.[14] As the interface κ varies inversely to δ,[26] the stronger thermal dissipation towards the $SrTiO_3$ substrate in PD.II′ results in a lower temperature gradient in the channel, posing an obstacle to the optimal performance.

As a key factor featuring the PTE-dominated self-powered photoresponse, S was extracted from:

$$V_{PTE} = \int -S\nabla T(x)\mathrm{d}x = S\Delta T \quad (4)$$

where V_{PTE} is the PTE-generate internal voltage and ΔT is the longitudinal temperature divergence in the channel under illumination.[26,29,48] ΔT was monitored using an IR camera when illuminated at the positive end of PD.I′. Fig. 5c shows the captured temperature landscape and the extracted temperature profile. By considering the thermal conduction across the channel and heat dissipation towards the substrate, the temperature profile can be expressed as:

$$\kappa\delta W\frac{\mathrm{d}^2T}{\mathrm{d}x^2} - GWT = -p'(x) \quad (5)$$

where G, W and p' refer to the heat transfer coefficient, the film width and the power dissipated per unit length, respectively; x is the radiant position, in which x = 0 and x = 3 mm are defined as the positive and negative ends, respectively.[50–52] Fig. 5c depicts the fitted temperature profile to the simplified one-dimensional expression of eqn (5):[50,51]

$$T(x) = \frac{P'}{W\sqrt{G\kappa\delta}}\mathrm{e}^{-\frac{x}{\lambda}} \quad (6)$$

The fairly good agreement between the experimental data and the simulation yields an estimation of ΔT = 6.75 K. The other parameter in eqn (4), V_{PTE} was extracted by:[53]

$$V_{PTE} = I_{PTE} \times R \quad (7)$$

$$\rho = R \times \frac{W\delta}{l} = R_{sheet} \times \delta \quad (8)$$

where I_{PTE} and l are the measured self-powered current and the channel length, respectively; ρ, R and R_{sheet} are the resistivity, resistance and sheet resistance of the Bi_2O_2Se layer, as have been reported elsewhere.[33] Consequently, the estimated S in PD.I′ is −127.8 μV K^{-1}, in perfect agreement with the reported values in Bi_2O_2Se,[26,29,48] indicating its applications in energy conversion and light harvesting.[32]

Band diagrams

Fig. 6 displays the energy band diagrams at thermal equilibrium of the $Bi_2O_2Se/SrTiO_3$ photodetectors. Under zero bias (Fig. 6a and b), the PTE effect governs the generation of photocarriers. ε_{PTE} orients from the hot end towards the cold, which leads to the consistent direction of I_{ph} and the electrode polarity under the light stimuli. When an external bias is imposed, coupling effects congruously govern the generation of photocarriers. The potentials triggered by the photon-electron

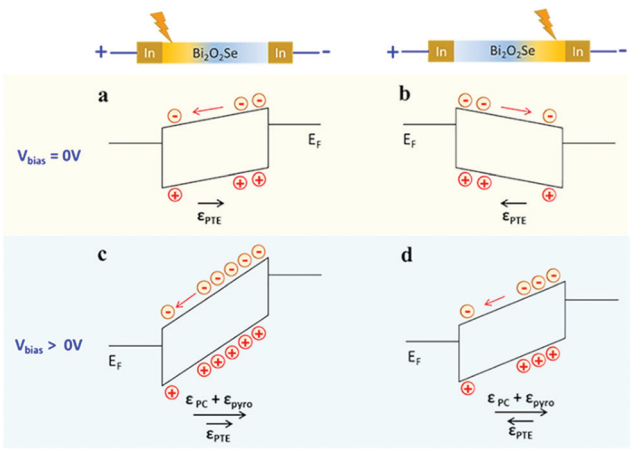

Fig. 6 Energy band diagrams of the $Bi_2O_2Se/SrTiO_3$ photodetectors when (a) illuminated at the positive end under 0 bias; (b) illuminated at the negative end under 0 bias; (c) illuminated at the positive end under positive bias; and (d) illuminated at the negative end under positive bias.

conversion (ε_{PC}) and the pyroelectric effect (ε_{pyro}) follow the direction of the external bias. Thus, when radiant at the positive end (Fig. 6c), all these effects promote the photoresponse, whereas under the negative-end optical exposure, ε_{PTE} suppresses I_{ph} (Fig. 6d). Among all the tested devices, the optimal figures-of-merit obtained under an external bias of 1 V reaches an R value of 12.62 A W^{-1}, an EQE value of 1424.08% and a D^* value of 1.51×10^9 Jones. As listed in Table S1 (ESI†), among all the as-grown Bi_2O_2Se photodetectors without transferring and external gating, the overall performance of our devices reaches a level of strong competiveness, especially considering their extra-large channel dimensions.[30] Hence, by scaling the channel or varying to a vertical-electrode configuration, enough room for performance optimization is foreseen in the $Bi_2O_2Se/SrTiO_3$ photodetectors.

Conclusions

We have demonstrated an interface-interaction assisted photoresponse in $Bi_2O_2Se/SrTiO_3$ heteroepitaxy, reaching an optimal performance involving a record-broad detection band of 365–1850 nm, an R value of 12.62 A W^{-1}, an EQE value of 1424.08% and a D^* value of 1.51×10^9 Jones. Photon detection is congruously governed by photoconductive, photogating, pyroelectric and PTE effects. Among them, pyroelectricity is attributed to the interfacial polarization with the dipole moments quantified by DFT calculation. This effect results in an overall performance enhancement, particularly the shortening of τ by a factor of $\sim$900. The emerging self-powered photoresponse results in a tunable magnitude and polarity of photocurrent as well as a high S of -127.8 μV K^{-1}. This photobehavior is governed by the PTE effect, and essentially affected by the interfacial phonon coupling and carrier scattering. Our study not only broadens the application of Bi_2O_2Se towards piezoelectronics, ferroelectronics, self-powered nanogenerators and optical communications, but also paves the way for exploring exotic phenomena at the epitaxial interface of Bi_2O_2Se and perovskite oxides, such as 2DEG, quantum transport, topological superconductivity and spin-dependent transport at magnetic tunnel junctions.

Conflicts of interest

There are no conflicts to declare.

Acknowledgements

This work was supported by the Shenzhen Science and Technology Project under Grant No. JCYJ20170412105400428 and JCYJ20180507182246321, the Natural Science Foundation of Shanghai (17ZR1436300) and the National Natural Science Foundation of China (11704395 and 11904236).

References

1 T. K. Agarwal, B. Soree, I. Radu, P. Raghavan, G. Iannaccone, G. Fiori, W. Dehaene and M. Heyns, *Sci. Rep.*, 2017, **7**, 5016.
2 H. Li, S. Ruan and Y. J. Zeng, *Adv. Mater.*, 2019, **31**, 1900065.
3 Z. Yang, H. Zhang, J. Xu, R. Ma, T. Sasaki, Y. Zeng, S. Ruan and H. Yanglong, *Natl. Sci. Rev.*, 2020, **7**, 841–848.
4 L. Huang, C. Chen, Z. Li, Y. Zhang, H. Zhang, J. Lu, S. Ruan and Y. J. Zeng, *Nanotechnology*, 2020, **31**, 162001.
5 Q. Wei, R. Li, C. Lin, A. Han, A. Nie, Y. Li, L. Li, Y. Cheng and W. Huang, *ACS Nano*, 2019, **13**, 13439–13444.
6 T. Tong, M. Zhang, Y. Chen, Y. Li, L. Chen, J. Zhang, F. Song, X. Wang, W. Zou, Y. Xu and R. Zhang, *Appl. Phys. Lett.*, 2018, **113**, 072106.
7 R. Xu, S. Wang, Y. Li, H. Chen, T. Tong, Y. Cai, Y. Meng, Z. Zhang, X. Wang and F. Wang, *IEEE Photonics Technol. Lett.*, 2019, **31**, 1056–1059.
8 C. Gong, J. Chu, S. Qian, C. Yin, X. Hu, H. Wang, Y. Wang, X. Ding, S. Jiang, A. Li, Y. Gong, X. Wang, C. Li, T. Zhai and J. Xiong, *Adv. Mater.*, 2020, 1908242.
9 C. Tan, M. Tang, J. Wu, Y. Liu, T. Li, Y. Liang, B. Deng, Z. Tan, T. Tu, Y. Zhang, C. Liu, J. H. Chen, Y. Wang and H. Peng, *Nano Lett.*, 2019, **19**, 2148–2153.
10 C. Chen, M. Wang, J. Wu, H. Fu, H. Yang, Z. Tian, T. Tu, H. Peng, Y. Sun, X. Xu, J. Jiang, N. B. M. Schröter, Y. Li, D. Pei, S. Liu, S. A. Ekahana, H. Yuan, J. Xue, G. Li, J. Jia, Z. Liu, B. Yan, H. Peng and Y. Chen, *Sci. Adv.*, 2018, **4**, eaat8355.
11 H. Xie, M. Liu, B. You, G. Luo, Y. Chen, B. Liu, Z. Jiang, P. K. Chu, J. Shao and X. Yu, *Small*, 2020, **16**, 1905208.
12 H. S. Kum, H. Lee, S. Kim, S. Lindemann, W. Kong, K. Qiao, P. Chen, J. Irwin, J. H. Lee, S. Xie, S. Subramanian, J. Shim, S. Bae, C. Choi, L. Ranno, S. Seo, S. Lee, J. Bauer, H. Li, K. Lee, J. A. Robinson, C. A. Ross, D. G. Schlom, M. S. Rzchowski, C.-B. Eom and J. Kim, *Nature*, 2020, **578**, 75–81.
13 Q. Y. Wang, Z. Li, W. H. Zhang, Z. C. Zhang, J. S. Zhang, W. Li, H. Ding, Y. B. Ou, P. Deng, K. Chang, J. Wen, C. L. Song, K. He, J. F. Jia, S. H. Ji, Y. Y. Wang, L. L. Wang, X. Chen, X. C. Ma and Q. K. Xue, *Chin. Phys. Lett.*, 2012, **29**, 037402.
14 J. F. Dayen, S. J. Ray, O. Karis, I. J. Vera-Marun and M. V. Kamalakar, *Appl. Phys. Rev.*, 2020, **7**, 011303.
15 S. Thiel, G. Hammerl, A. Schmehl, C. W. Schneider and J. Mannhart, *Science*, 2006, **313**, 1942–1945.
16 Y. Z. Chen, N. Bovet, F. Trier, D. V. Christensen, F. M. Qu, N. H. Andersen, T. Kasama, W. Zhang, R. Giraud, J. Dufouleur, T. S. Jespersen, J. R. Sun, A. Smith, J. Nygård, L. Lu, B. Büchner, B. G. Shen, S. Linderoth and N. Pryds, *Nat. Commun.*, 2013, **4**, 1371.
17 Y.-J. Zeng, N. Gauquelin, D.-Y. Li, S.-C. Ruan, H.-P. He, R. Egoavil, Z.-Z. Ye, J. Verbeeck, J. Hadermann, M. J. Van Bael and C. Van Haesendonck, *ACS Appl. Mater. Interfaces*, 2015, **7**, 22166–22171.
18 A. Zhao, H. Li, X. Hu, C. Wang, H. Zhang, J. Lu, S. Ruan and Y. Zeng, *J. Phys. D: Appl. Phys.*, 2020, **53**, 293002.
19 A. Ohtomo and H. Y. Hwang, *Nature*, 2004, **427**, 423–427.
20 S. W. Lee, *J. Nanomater.*, 2016, 1–9.
21 Y. Chen and R. J. Green, *Adv. Mater. Interfaces*, 2019, **6**, 1900547.
22 N. Erdman, K. R. Poeppelmeier, M. Asta, O. Warschkow, D. E. Ellis and L. D. Marks, *Nature*, 2002, **419**, 55–58.

23 E. Meirzadeh, D. V. Christensen, E. Makagon, H. Cohen, I. Rosenhek-goldian, E. H. Morales, A. Bhowmik, J. M. G. Lastra, A. M. Rappe, D. Ehre, M. Lahav, N. Pryds and I. Lubomirsky, *Adv. Mater.*, 2019, 1904733.
24 H. Li, X. Xu, Y. Zhang, R. Gillen, L. Shi and J. Robertson, *Sci. Rep.*, 2018, **8**, 10920.
25 X. Zhang, Y. Qiu, D. Ren and L.-D. Zhao, *Ann. Phys.*, 2019, 1900340.
26 L. Pan, L. Zhao, X. Zhang, C. Chen, P. Yao, C. Jiang, X. Shen, Y. Lyu, C. Lu, L.-D. Zhao and Y. Wang, *ACS Appl. Mater. Interfaces*, 2019, **11**, 21603–21609.
27 T. Yang, X. Li, L. Wang, Y. Liu, K. Chen, X. Yang, L. Liao, L. Dong and C.-X. Shan, *J. Mater. Sci.*, 2019, **54**, 14742–14751.
28 P. Luo, F. Zhuge, F. Wang, L. Lian, K. Liu, J. Zhang and T. Zhai, *ACS Nano*, 2019, **13**, 9028–9037.
29 T. Tong, Y. Chen, S. Qin, W. Li, J. Zhang, C. Zhu, C. Zhang, X. Yuan, X. Chen, Z. Nie, X. Wang, W. Hu, F. Wang, W. Liu, P. Wang, X. Wang, R. Zhang and Y. Xu, *Adv. Funct. Mater.*, 2019, 1905806.
30 X. Liu, R. Li, C. Hong, G. Huang, D. Pan, Z. Ni, Y. Huang, X. Ren, Y. Cheng and W. Huang, *Nanoscale*, 2019, **11**, 20707–20714.
31 H. Yang, C. Tan, C. Deng, R. Zhang, X. Zheng, X. Zhang, Y. Hu, X. Guo, G. Wang, T. Jiang, Y. Zhang, G. Peng, H. Peng, X. Zhang and S. Qin, *Small*, 2019, 1904482.
32 X. Lu, P. Jiang and X. Bao, *Nat. Commun.*, 2019, **10**, 138.
33 Y. Song, Z. Li, H. Li, S. Tang, G. Mu, L. Xu, W. Peng, D. Shen, Y. Chen, X. Xie and M. Jiang, *Nanotechnology*, 2020, **31**, 165704.
34 J. Wu, Y. Liu, Z. Tan, C. Tan, J. Yin, T. Li, T. Tu and H. Peng, *Adv. Mater.*, 2017, **29**, 1704060.
35 J. Hutter, M. Iannuzzi, F. Schiffmann and J. VandeVondele, *Wiley Interdiscip. Rev.: Comput. Mol. Sci.*, 2014, **4**, 15–25.
36 S. Goedecker, M. Teter and J. Hutter, *Phys. Rev. B: Condens. Matter Mater. Phys.*, 1996, **54**, 1703–1710.
37 S. Grimme, *J. Comput. Chem.*, 2006, **27**, 1787–1799.
38 J. VandeVondele and J. Hutter, *J. Chem. Phys.*, 2007, **127**, 114105.
39 J. Vandevondele, M. Krack, F. Mohamed, M. Parrinello, T. Chassaing and J. Hutter, *Comput. Phys. Commun.*, 2005, **167**, 103–128.
40 C. Hartwigsen, S. Goedecker and J. Hutter, *Phys. Rev. B: Condens. Matter Mater. Phys.*, 1998, **58**, 3641–3662.
41 Q. Fu, C. Zhu, X. Zhao, X. Wang, A. Chaturvedi, C. Zhu, X. Wang, Q. Zeng, J. Zhou, F. Liu, B. K. Tay, H. Zhang, S. J. Pennycook and Z. Liu, *Adv. Mater.*, 2019, **31**, 1804945.
42 Y. Y. Lv, L. Xu, S. T. Dong, Y. C. Luo, Y. Y. Zhang, Y. B. Chen, S. H. Yao, J. Zhou, Y. Cui, S. T. Zhang, M. H. Lu and Y. F. Chen, *Phys. Rev. B*, 2019, **99**, 195143.
43 J. Li, Z. Wang, J. Chu, Z. Cheng, P. He, J. Wang, L. Yin, R. Cheng, N. Li, Y. Wen and J. He, *Appl. Phys. Lett.*, 2019, **114**, 151104.
44 D. Ehre, E. Mirzadeh, O. Stafsudd and I. Lubomirsky, *Ferroelectrics*, 2014, **472**, 41–49.
45 F. Yang, R. Wang, W. Zhao, J. Jiang, X. Wei, T. Zheng, Y. Yang, X. Wang, J. Lu and Z. Ni, *Appl. Phys. Lett.*, 2019, **115**, 193103.
46 J. P. Perdew, K. Burke and M. Ernzerhof, *Phys. Rev. Lett.*, 1997, **78**, 1396.
47 N. M. Gabor, J. C. W. Song, Q. Ma, N. L. Nair, T. Taychatanapat, K. Watanabe, T. Taniguchi, L. S. Levitov and P. Jarillo-Herrero, *Science*, 2011, **334**, 648–653.
48 D. Guo, C. Hu, Y. Xi and K. Zhang, *J. Phys. Chem. C*, 2013, **117**, 21597–21602.
49 Z. Wu, G. Liu, Y. Wang, X. Yang, T. Wei, Q. Wang, J. Liang, N. Xu, Z. Li, B. Zhu, H. Qi, Y. Deng and J. Zhu, *Adv. Funct. Mater.*, 2019, 1906639.
50 Y. Wang, Y. Niu, M. Chen, J. Wen, W. Wu, Y. Jin, D. Wu and Z. Zhao, *ACS Photonics*, 2019, **6**, 895–903.
51 K. J. Erikson, X. He, A. A. Talin, B. Mills, R. H. Hauge, T. Iguchi, N. Fujimura, Y. Kawano, J. Kono and F. Léonard, *ACS Nano*, 2015, **9**, 11618–11627.
52 E. Pop, D. A. Mann, K. E. Goodson and H. Dai, *J. Appl. Phys.*, 2007, **101**, 093710.
53 V. Shautsova, T. Sidiropoulos, X. Xiao, N. A. Güsken, N. C. G. Black, A. M. Gilbertson, V. Giannini, S. A. Maier, L. F. Cohen and R. F. Oulton, *Nat. Commun.*, 2018, **9**, 5190.

